Review of Scientific Instruments

Room temperature "*optical nanodiamond hyperpolarizer*": Physics, design, and operation

Cite as: Rev. Sci. Instrum. **91**, 023106 (2020); https://doi.org/10.1063/1.5131655
Submitted: 14 October 2019 . Accepted: 22 January 2020 . Published Online: 25 February 2020

A. Ajoy, R. Nazaryan, E. Druga, K. Liu, A. Aguilar, B. Han, M. Gierth, J. T. Oon, B. Safvati, R. Tsang, J. H. Walton, D. Suter, C. A. Meriles, J. A. Reimer, and A. Pines

Review of Scientific Instruments ARTICLE scitation.org/journal/rsi

Room temperature "*optical nanodiamond hyperpolarizer*": Physics, design, and operation

Cite as: Rev. Sci. Instrum. 91, 023106 (2020); doi: 10.1063/1.5131655
Submitted: 14 October 2019 • Accepted: 22 January 2020 •
Published Online: 25 February 2020

A. Ajoy,[1,a)] R. Nazaryan,[1] E. Druga,[1] K. Liu,[1] A. Aguilar,[1] B. Han,[1] M. Gierth,[1] J. T. Oon,[1] B. Safvati,[1] R. Tsang,[1] J. H. Walton,[2] D. Suter,[3] C. A. Meriles,[4] J. A. Reimer,[5] and A. Pines[1]

AFFILIATIONS

[1]Department of Chemistry and Materials Science Division, Lawrence Berkeley National Laboratory, University of California Berkeley, Berkeley, California 94720, USA
[2]Nuclear Magnetic Resonance Facility, University of California Davis, Davis, California 95616, USA
[3]Fakultat Physik, Technische Universitat Dortmund, D-44221 Dortmund, Germany
[4]Department of Physics and CUNY-Graduate Center, CUNY-City College of New York, New York, New York 10031, USA
[5]Department of Chemical and Biomolecular Engineering, and Materials Science Division, Lawrence Berkeley National Laboratory, University of California, Berkeley, California 94720, USA

[a)]**Author to whom correspondence should be addressed:** ashokaj@berkeley.edu

ABSTRACT

Dynamic Nuclear Polarization (DNP) is a powerful suite of techniques that deliver multifold signal enhancements in nuclear magnetic resonance (NMR) and MRI. The generated athermal spin states can also be exploited for quantum sensing and as probes for many-body physics. Typical DNP methods require the use of cryogens, large magnetic fields, and high power microwave excitation, which are expensive and unwieldy. Nanodiamond particles, rich in Nitrogen-Vacancy (NV) centers, have attracted attention as alternative DNP agents because they can potentially be optically hyperpolarized at room temperature. Here, unraveling new physics underlying an optical DNP mechanism first introduced by Ajoy *et al.* [Sci. Adv. **4**, eaar5492 (2018)], we report the realization of a miniature "optical nanodiamond hyperpolarizer," where ^{13}C nuclei within the diamond particles are hyperpolarized via the NV centers. The device occupies a compact footprint and operates at room temperature. Instrumental requirements are very modest: low polarizing fields, low optical and microwave irradiation powers, and convenient frequency ranges that enable miniaturization. We obtain the best reported optical ^{13}C hyperpolarization in diamond particles exceeding 720 times of the thermal 7 T value (0.86% bulk polarization), corresponding to a ten-million-fold gain in averaging time to detect them by NMR. In addition, the hyperpolarization signal can be background-suppressed by over two-orders of magnitude, retained for multiple-minute long periods at low fields, and deployed efficiently even to ^{13}C enriched particles. Besides applications in quantum sensing and bright-contrast MRI imaging, this work opens possibilities for low-cost room-temperature DNP platforms that relay the ^{13}C polarization to liquids in contact with the high surface-area particles.

I. INTRODUCTION

Dynamic Nuclear Polarization (DNP),[1] the process of transferring spin polarization from electrons to surrounding nuclei, *hyperpolarizing* them to levels of large fictitious magnetic fields,[2] has been a burgeoning field with applications across numerous disciplines. For instance, the versatile, noninvasive, and chemically specific spectroscopic and imaging techniques[3] of NMR and MRI can see their signals enhanced by orders of magnitude through the use of DNP.[4] Moreover, hybrid electron–nuclear quantum sensing platforms, for instance, gyroscopes,[5–7] can see sensitivity gains through nuclear hyperpolarization. Finally, the generated *athermal* spin states provide valuable physical testbeds to study many body quantum dynamics, spin transport, and localization in dipolar coupled spin systems.[8,9] However, conventional methods of DNP[10–12] involve the use of cryogenic conditions ($\lesssim$1 K) and high magnetic fields ($\gtrsim$3 T) in order to first generate the electron polarization. In some applications, this limits the

hyperpolarization throughput due to several hour-long relaxation times and the necessity to cool down the sample every time. In many respects, this restricts wider real-world deployment, given the high cost of setup and maintenance of cryogenic polarizer devices. There is, therefore, a strong desire for inexpensive room-temperature DNP platforms that can potentially retrofit the existing NMR/MRI infrastructure and provide hyperpolarization generation "at source."[13]

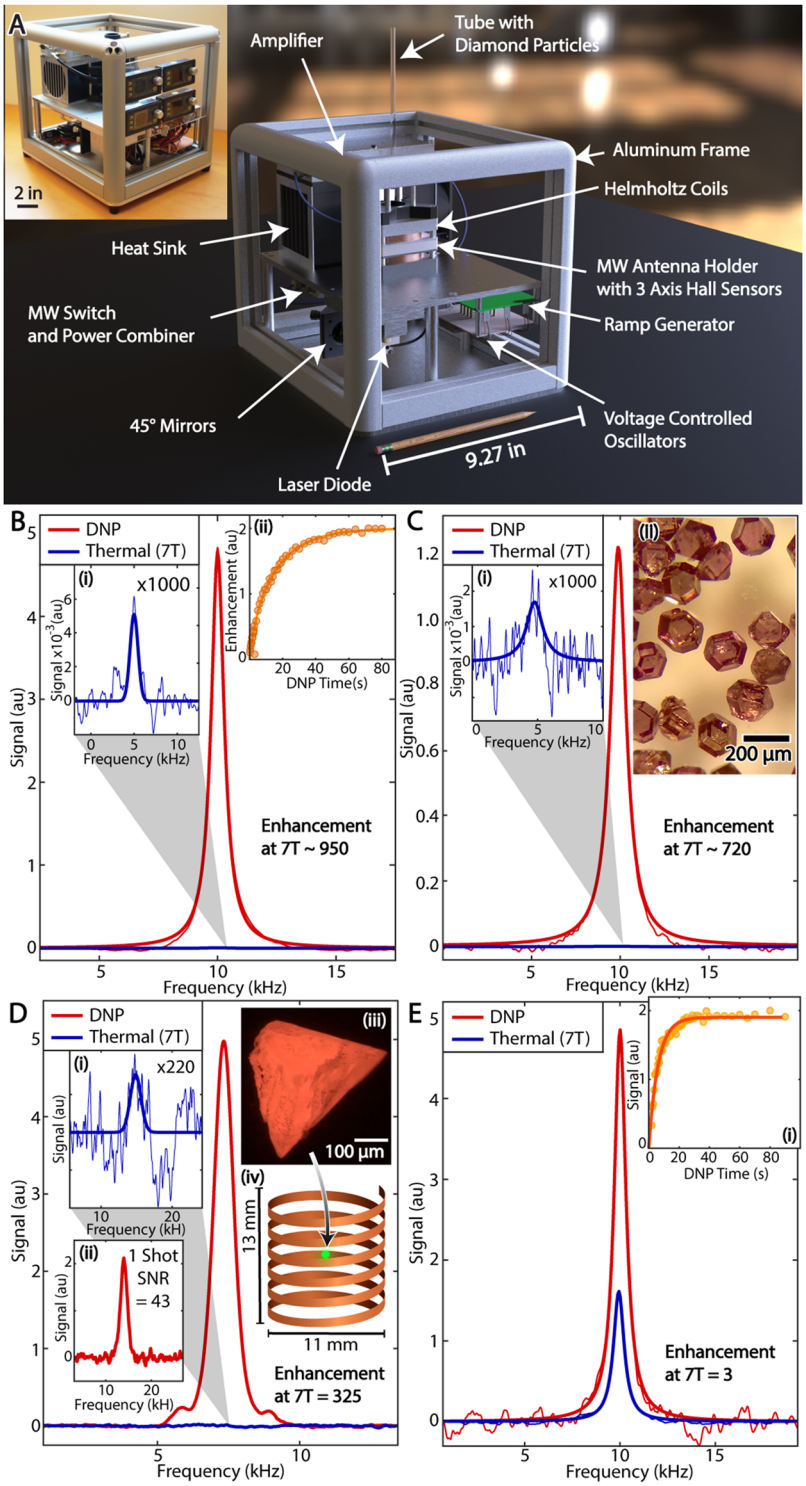

FIG. 1. Nanodiamond hyperpolarizer. (a) *Rendered model*. Compact device (<10 in. cubical edge) containing all optical, microwave (MW), and control components generates hyperpolarized diamond particles at a high throughput ≈20 mg/min. *Inset:* Photograph of the constructed device (see Fig. 2). See Ref. 25 for a video of operation. [(b)–(d)] *Results using a hyperpolarizer device* at 38 mT. ^{13}C signals are measured by transfer to a 7 T NMR magnet. Red (blue) lines show the DNP signal (7 T thermal signal, zoomed-in insets). (b) *Single crystal* DNP demonstrating enhancement $\varepsilon \approx 950$. Here, DNP and thermal are with 10 and 120 averages, respectively. Hyperpolarization buildup, typical for most samples, occurs under 60 s. (c) *Microcrystalline diamond powder* DNP with best reported polarization enhancements $\varepsilon \approx 720$. Here, DNP and thermal are with 1 and 120 averages, respectively. *Inset:* Particle micrograph. (d) *Single particle* DNP of a 10% ^{13}C enriched and ~400 μm sized single particle showing $\varepsilon = 325$ over 7 T. Here, DNP and thermal are both 512 averages. Inset (ii): Single shot DNP signal with signal-to-noise ratio (SNR) ≈43 in a 1235 mm^3 NMR coil. Inset (iii): Particle micrograph with fluorescence from NV centers. Inset (iv): Schematic of the detection coil. We obtain large single shot signals despite poor sample fill-factors ~10^{-6}. (c) *Nanodiamond* DNP with commercial 100 nm NDs in solution, showing $\varepsilon = 3$ over 7 T. Here, DNP and thermal are with 10 and 512 averages, respectively. *Inset:* Hyperpolarization buildup curve.

In recent years, the development of defect centers in wide bandgap semiconductors has proffered them as interesting candidates for optical room temperature hyperpolarization. This leverages the fact that electronic spin defects in these systems can be optically initialized.[14] Nanodiamond particles endowed with Nitrogen Vacancy (NV) defect centers have been suggested as one such compelling hyperpolarization platform.[15–18] The NV electrons can be optically polarized with modest resources, the polarization transferred to ^{13}C nuclei in the lattice, and subsequently relayed to nuclei in a liquid in contact with the high surface-area ($\gtrsim$10 m^2/g) particle surfaces.[19,20] Hyperpolarized particulate diamonds portend other applications: powdered samples represent the optimal size configuration to fill a sensor volume and maximize the number of spins available for quantum sensing.[7] They also engender possibilities for quantum sensors constructed from single levitating hyperpolarized diamond particles.[21] Finally, nanodiamonds are fluorescent and non-toxic,[22–24] and hyperpolarization opens pathways for imaging these particles in dual-modality consisting of optical and MRI imaging simultaneously.

In recent work, we had demonstrated the first experimental technique for the generation of optically hyperpolarized diamond particles.[20] We relied on an unconventional DNP regime operational at low fields and exhibited hyperpolarization of the ^{13}C nuclei irrespective of the orientation of the individual crystallites. In this paper, we refine the experimental conditions for the optimal generation of hyperpolarization by focusing on the field dependence of the underlying DNP process. We demonstrate that this optical DNP mechanism is fully orientation independent and low-field only, occurring at polarization fields B_{pol} = 1–70 mT, and low-enough to be generated with the simplicity of a refrigerator magnet. Besides the magnetic field, we demonstrate that the DNP mechanism affords benign requirements for optical and microwave (MW) excitation.

Leveraging this new physics, we construct a room temperature "optical nanodiamond hyperpolarizer" device that can produce ^{13}C hyperpolarization in diamond particles with a high throughput (≈20 mg/min). Figure 1(a) shows a photograph and the rendered view of the device. Figure 2 (Multimedia view) shows the construction of the device, and Ref. 25 shows a video of it in operation. It has an ultracompact form-factor (~10 in. edge) that houses all the electronic, MW, and optical components required to produce hyperpolarization in diamond particles at room temperature. The device is portable enough to "*DNP-retrofit*" any magnet system. We have deployed two such devices across 7 T and 9.4 T (imaging) magnets at UC Berkeley and UC Davis. We emphasize that the ability to construct such a hyperpolarization device is itself somewhat surprising and due to a confluence of factors unique to the physics of optically pumped quantum defects. In this paper, we uncover these features and also highlight engineering design aspects that make possible the miniaturizable device.

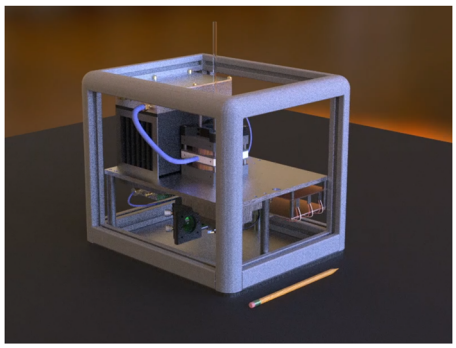

FIG. 2. Video showing rendered construction of the hyperpolarizer device and all its component parts. Multimedia view: https://doi.org/10.1063/1.5131655.1

II. HYPERPOLARIZATION RESULTS

In Figs. 1(b)–1(e), we demonstrate representative results using our device on various types of diamond samples. The ^{13}C hyperpolarization enhancements ε are evaluated with respect to the thermal Boltzmann level at 7 T, corresponding to a time acceleration for spectroscopy or imaging $t_{\mathrm{acc}} \approx \varepsilon^2 \frac{T_1(7T)}{T_1(B_{\mathrm{pol}})}$. The key advantage of optical hyperpolarization is that the enhancement factor is not theoretically bounded, unlike in conventional methods wherein $\varepsilon \leq \gamma_e/\gamma_n$, the ratio of the electronic and nuclear gyromagnetic ratios. For a typical single crystal sample (3.24 mm × 3.24 mm × 0.3 mm), we obtain in Fig. 1(b) large DNP enhancements ε = 950 corresponding to a ^{13}C polarization level ~1.1% and larger than ten-million fold acceleration ($t_{\mathrm{acc}} \approx 5.3 \times 10^7$) in averaging time. For the randomly oriented microcrystalline diamond powder [see Fig. 1(b)], we obtain the best reported polarization with ε = 720, corresponding to a ^{13}C polarization level ~0.86%, and an acceleration factor $t_{\mathrm{acc}} \approx 9.8 \times 10^6$. We note that while cyrogenic DNP provides larger enhancements, a majority of the obtained hyperpolarization is lost upon sample transfer outside the cryostat.[26,27] The polarization in Fig. 1(c) is thus ultimately slightly stronger, can be obtained at a higher throughput, and is optically replenishable. Moreover, due to the DNP being carried out under ambient conditions, the hyperpolarization enhancements can be maintained even when the particles are immersed in solution, for instance, common solvents, such as water, dimethyl sulfoxide (DMSO), and oil, and biologically relevant liquids such as saline and blood (see the supplementary material). The microcrystals in Fig. 1(c) are employed for all the other experiments reported in this manuscript.

Given the high polarization gain [see Fig. 1(d)], we are also able to detect a *single* hyperpolarized diamond microparticle with a single-shot SNR >40 [see Fig. 1(d)(ii)]. There is substantial room for further signal enhancements because the particle herein occupies a very small part of the detection coil (~1 cm cylinder) corresponding to a sample filling-factor for NMR detection ≈6×10^{-6}. Such high signals portend quantum sensing applications constructed out of hybrid spin-mechanical systems in single microparticles.[28,29] Finally, Fig. 1(e) demonstrates results with the device on a large mass ≈42 mg of commercially available 100 nm nanodiamond particles in solution (see the Appendix). We ascribe the lower polarization herein to be limited by the material properties and finite optical penetration through the colloidal suspension. In Ref. 30, we study these material conditions affecting hyperpolarization and demonstrate methods by which the diamond particles can be rendered more suitable for optical DNP.

III. TECHNOLOGY ENABLING MINIATURIZATION

Hyperpolarization is achieved by the continuous application of laser and frequency swept MW irradiation at low background fields $\mathbf{B}_{pol}$[20] [see Fig. 3(b)]. The laser polarizes NV centers (we estimate to >10%) to the $m_s = 0$ sublevel, and the MWs transfer the polarization to the ^{13}C nuclei. In practice, we use a combination of three cascaded MW sweepers for greater signal enhancement.[31] Refining and expanding on the work in Ref. 20, we begin by first summarizing the key results of this paper. Miniaturized hyperpolarization devices are possible because of a confluence of four factors stemming from the underlying DNP mechanism.

A. Field

We observe that hyperpolarization is optimum at a low polarizing field $\mathbf{B}_{pol} \approx 38$ mT. Such low fields are simple to produce a miniature footprint either through a permanent magnet or a simple magnetic coil. There are no requirements on field alignment. Given that we are dealing with powders with inherently broadened electronic spectra, there are very little constraints on field homogeneity. In principle, we expect that DNP can proceed even in inhomogeneous settings with $\Delta B_{pol} \sim B_{pol}$, while in our experimental demonstrations, $\Delta B_{pol}/B_p \approx 0.1$. Moreover, due to spin reorientation during sample shuttling, the polarization field does not need to be aligned with the detection NMR field. This allows installation and retrofits of the device anywhere in the vicinity of detection magnets.

B. Optics

The laser excitation required is of very low power since the NVs need to be polarized only once every T_{1e} relaxation cycle. We estimate the optical power ≈30–400 mW/mm^3 depending on the number of laser sources employed. We contrast this with higher optical powers ~ 1 mW/(μm)^2 typically required for quantum sensing experiments employing optical NV center readout. There are no requirements on the excitation wavelength (510 nm $\lesssim \lambda \lesssim$ 575 nm), linewidth, or mode quality. Indeed, diffuse irradiation through multimode optical fibers is sufficient. The optical excitation is in completely *cw*-mode, requiring no synchronization or pulsing infrastructure [e.g., acousto-optic modulators (AOMs)]. This facilitates the use of (one or multiple) inexpensive miniaturizable laser diode excitation sources.

C. Microwaves

The MW power required is exceedingly low (≈2 mW/mm^3). There is a relatively weak dependence of the DNP enhancement on MW power,[20] making the hyperpolarization robust to MW inhomogeneity. We estimate the electron Rabi frequency $\Omega_e \lesssim 100$ kHz and a MW inhomogeneity of ≈12% from the 4 mm loop antenna in our device (Supplementary material). Moreover, since the MWs are chirped, they are inherently robust against carrier phase noise, especially when compared to more conventionally pulse-based DNP approaches.[16] Our MW excitation linewidth, for instance, is rather

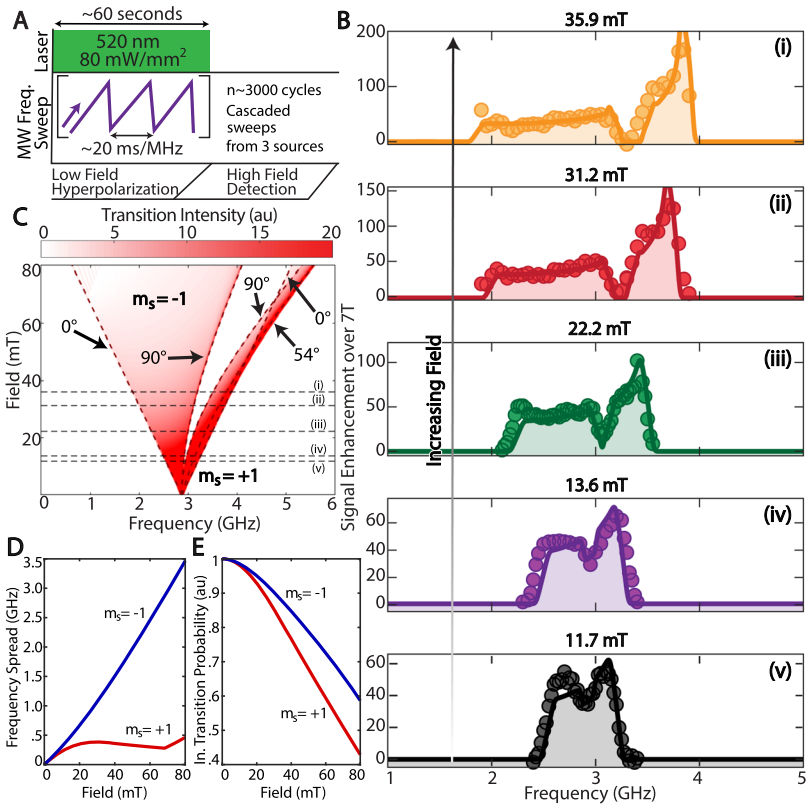

FIG. 3. Fully orientation independent hyperpolarization. (a) *DNP pulse sequence* at a low-field involving simultaneous laser and chirped MW irradiation over the NV center electron spin resonance (ESR) spectrum. DNP enhancements are quantified by NMR detection at 7 T. (b) *Electronic spectra mapped* via ^{13}C *DNP* on 200 μm particles [Fig. 1(c)]. Hyperpolarized ^{13}C NMR is performed on narrow 100 MHz frequency windows (points) to map the underlying NV ESR spectrum at various fields (*i*)–(*v*). Solid lines are fits to the calculated spectrum [dashed linecuts in (c)] and show good agreement. Panels illustrate that *all* orientations of the particles contribute constructively to hyperpolarization, all with the same sign. (c) *Simulated NV electronic spectra*, shown as a function of field, due to varying orientations (ϑ) of N-V axes in crystallites in the diamond powder with respect to the polarizing field $\mathbf{B}_{pol}$. Shading is proportional to electronic transition intensities $P(\vartheta, B_{pol})$. Exact orientations that contribute to the extrema of the patterns in $m_s = \pm 1$ manifolds are indicated by arrows and the red dashed lines. (d) *Frequency spread* in either electronic manifold, showing an approximately linear fan out of transitions in the $m_s = -1$ branch, as opposed to being constant (≈400 MHz) in the $m_s = +1$ branch at moderate fields. (e) *Integrated transition intensity* $\mathcal{T}(B_{pol})$ averaged over all orientations of the powder, indicating that the net transition intensity falls with the increasing field.

broad (≈10 MHz). The frequency sweep band ($\mathcal{B}$ ~3.64–4 GHz) at B_{pol} = 38 mT lies in the commercial WiMAX regime, and the use of commercial chip scale voltage controlled oscillator (VCO) sources ubiquitously available in this band simplifies miniaturization. Broadband antennas can deliver the MWs, with no requirement for a MW cavity or a sophisticated transmission infrastructure. MW chirp repetition rates are slow $\omega_r \approx 147$ Hz, robust $\Delta\omega_r \approx 53$ Hz, and to a good approximation independent of the polarizing magnetic field. This allows a simple frequency sweep infrastructure and the cascading of multiple MW sources to boost DNP efficiency.[31]

D. Polarization sign

Sweeps over every part of the NV electronic spectrum produce hyperpolarization that constructively adds to the *same* polarization sign. The MW sweep bands can be optimally tuned to the simulated electronic spectral widths at any given B_{pol} field to optimize final hyperpolarization enhancements.

These attributes are consequences of the underlying DNP mechanism. We refer the reader to more detailed expositions elsewhere[32] but briefly mention that DNP occurs when the nuclear Larmor frequency $\omega_L = \gamma_n B_{pol} \approx 10$–700 kHz is smaller than the hyperfine coupling A, i.e., $\omega_L \lesssim |A|$. Here, γ_n is the ^{13}C gyromagnetic ratio, $\gamma_n \approx 10.7$ kHz/mT. The swept MWs excite a sequential set of Landau–Zener (LZ) crossings between the electron–nuclear spin states in the rotating frame, and this drives a "ratchet" type process for polarization transfer. This, at once, results in lower laser and microwave power requirements: MW power should be low enough to maintain adiabaticity of the LZ traversals and the laser excitation of sufficiently low power to not break the coherence of the polarization transfer process. Indeed, at optical powers that we operate under, the NV electronic repolarization occurs at a rate $\approx 1/T_{1e}$ and takes place predominantly during the long intervals far away from the LZ anti-crossings.[20,32]

IV. ORIENTATION INDEPENDENT HYPERPOLARIZATION

In Ref. 20, we had observed that every part of the NV electronic spectrum contributes to DNP and that the sign of the resulting ^{13}C polarization depends on the direction of the sweep. While this was a strong indication that DNP was excited for all orientations, it was not immediately evident that polarization builds up equally efficiently in every orientation of random crystallites in the diamond powder. In this paper, we perform new experiments that quantitatively answer this question in the affirmative. This stands in contrast to other proposals for nanodiamond DNP,[33] where only spins in a narrow cone are polarized. These results also point out to a simple means to optimize hyperpolarization enhancements at any given polarizing field B_{pol}.

We perform experiments sweeping MWs in narrow 100 MHz windows using the obtained ^{13}C DNP enhancements to report on the underlying NV ESR spectra.[20] We employ a Helmholtz coil [see Fig. 4(d)] within the polarizer device to generate varying polarization fields in a background fringe field of a 7 T NMR spectrometer. Embedded chip-scale Hall sensors measure the field along three axes, and the vector fields are reported in Fig. 3(b). As expected, the spectra become wider at higher fields. The key new result in this paper, however, is contained in the solid lines that provide good fits to the experimental data. These fits involve a single free parameter (overall amplitude) and are derived from a simple model of the NV center electronic spectrum alone, without having to include hyperfine couplings to the ^{13}C nuclei. The experiments reveal, therefore, that the ^{13}C hyperpolarization fully follows the underlying NV electron density of states, pointing out to complete DNP orientation independence. They also reflect that it is the weakly coupled ^{13}C nuclei that are predominantly polarized.

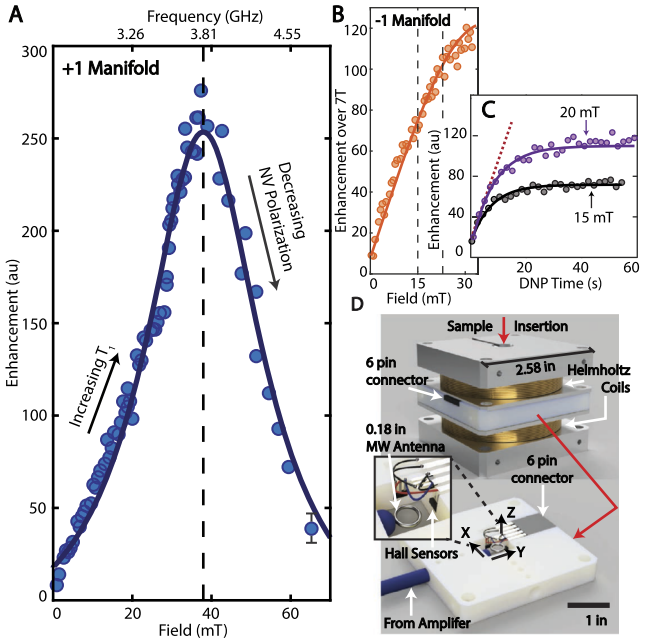

FIG. 4. Field dependent DNP profile. (a) *Field dependence* of maximum hyperpolarization enhancements in 1–70 mT range for the m_s = +1 NV manifold. Experiments are performed at optimal MW sweep rates at each field (see the Appendix). We observe a steep decrease in DNP efficiency at ultralow fields <20 mT and at fields >50 mT, and a sharp optimum at ≈38 mT. We ascribe this to be due the interplay between low ^{13}C lifetimes at low fields and inefficient optical polarization in a powder at high fields. Center of MW sweep bands are shown on top axis. The solid line is a guide to the eye. Error bar ≈11% is shown representatively on the last point. (b) Similar experiments performed on m_s = −1 manifold. (c) Comparison of polarization buildup curves at 15 mT and 20 mT, showing longer saturation times for the latter, a reflection of longer nuclear relaxation times. Red dashed line shows the identical rate of polarization buildup at both fields. (d) *Helmholtz coil* placed over the MW loop antenna onboard nanodiamond hyperpolarizer device (see also Fig. 8) can be used to apply the polarizing field in a variety of environments of NMR detection magnets. *Inset:* Three Hall probes measure the *vector* magnetic field in close proximity to the MW antenna and sample.

To be more specific, Fig. 3(c) shows simulated NV ESR spectra at various fields, where the shading color is proportional to the transition intensity under applied MW excitation. The solid lines in Fig. 3(b) are line-cuts in this graph (dashed lines). We start with the spin-1 NV center Hamiltonian $\mathcal{H}(\vartheta) = \Delta S_z^2 + \gamma_e B_{pol}(S_x \sin\vartheta + S_z \cos\vartheta)$, where Δ = 2.87 GHz is the zero-field splitting, γ_e = 28 MHz/mT is the electron gyromagnetic ratio, and S_j are Pauli matrices. We calculate the eigenvectors such that $\mathcal{H}|v_k\rangle = E_k|v_k\rangle$ and obtain the transition intensities $P(\vartheta, B_{pol})$

$\sim\sum_{k<\ell}\sum_m|\langle v_k|S_m|v_\ell\rangle|^2[\langle v_k|\rho|v_k\rangle-\langle v_\ell|\rho|v_\ell\rangle]$, where the first factor quantifies the transition probabilities in the randomly oriented powder where $m \in \{x, y, z\}$. The second factor describes the population difference between the eigenstates, with $\rho = \mathbb{1} - S_z^2/3$. The predicted spectra are then calculated by assuming a Gaussian spectral width ≈28 MHz (corresponding to a field inhomogeneity ≈1 mT) for each transition, averaging the effective $P(\vartheta)$ over 300 random orientations in the powder, and then convoluting the result by the sweep window. The extremities of the spectra at low fields are easy to identify, at frequencies $\Delta \mp \gamma_e B_{\rm pol}$, as originating from the crystallites aligned with $B_{\rm pol}$ ($\vartheta = 0°$) in the $m_s = \mp 1$ manifolds. Similarly, the perpendicular ($\vartheta = 90°$) orientations occur more centrally in the powder pattern at frequencies $\frac{1}{2}[\Delta + \sqrt{\Delta^2 + (2\gamma_e B_{\rm pol})^2}]$ and $[\sqrt{\Delta^2 + (2\gamma_e B_{\rm pol})^2}]$, respectively. The region in-between the two manifolds has no electronic density of states and consequently produces no DNP enhancements, resulting in the apparent "holes" around 3 GHz in Fig. 3(b).

This simple model now allows a simple means to optimize the DNP enhancement. First, knowledge of the *vector* polarizing field, for instance, through Hall probes embedded in the device near the sample, can point out to the exact frequency band $\mathcal{B}$ for the MWs to sweep over. This ensures that the applied microwaves are sweeping over electrons at every time instant during the full polarization period (constrained by nuclear T_1). Moreover, as Fig. 3(d) demonstrates, the frequency spread in the $m_s = -1$ manifold grows approximately linearly with field, while in the $m_s = +1$ manifold, it saturates after an initial quadratic rise. Since there is a relative reduction of electron density of states per unit frequency bandwidth in the $m_s = -1$ manifold as opposed to the $m_s = +1$ manifold, higher DNP enhancements are obtained by MW sweeps over the $m_s = +1$ branch. This is also evident in the experiments in Fig. 3(b). At 36 mT, for instance, a single 100 MHz sweep window in the $m_s = +1$ manifold can provide DNP enhancements approaching 200 over 7 T [Fig. 3(b)].

As a result, the excited DNP is highly robust to generate. (i) Any part of the frequency band can be swept over to produce hyperpolarization, in contrast to conventional DNP (solid/cross-effects), where misplaced frequency windows can lead to destructive polarization generation between various spin packets. (ii) Given that the ESR spectrum is orientationally broadened to start with, field inhomogeneities do not significantly alter the DNP enhancements. We estimate an inhomogeneity of 2 mT over the sample volume (see the supplementary material) in our device. (iii) Moreover, since the NV electrons are quantized along randomly oriented axes in the powder, $\mathbf{B}_{\rm pol}$ can be applied in any direction. It can hence be generated by a vector combination of a single-axis Helmholtz coil and the magnet fringe field. These favorable settings enable the simple installation of the device in the vicinity of detection magnets—one simply "dials-up" the current in the Helmholtz coil such that the net vector field seen by the sample is the optimal value, $|\mathbf{B}_{\rm pol}| \approx 38$ mT.

V. HYPERPOLARIZATION FIELD PROFILE

We now turn our attention to the field dependence of the DNP enhancements. Determining an *a priori* analytical model from microscopics of the "DNP ratchet"[20,32] is challenging since there are several factors at play simultaneously: different orientations in the powder, a continuum of hyperfine couplings within the diamond lattice, as well as always operational nuclear spin diffusion and relaxation effects. However, one could generally state that the DNP mechanism is operational at low fields, since the critical hierarchy that we rely on, $\omega_L \lesssim |A|$, flips at higher fields. Indeed, in this regime, the mechanism will transition to the more conventional Integrated Solid Effect (ISE),[34] with several contrasting features.

Before going forward, we do emphasize, however, that these low-field regimes ($\lesssim$70 mT) have been traditionally inaccessible to DNP since typically electron polarization is also generated through a Boltzmann distribution at cryogenic conditions at high fields. Indeed, materials such as the diamond NV center provide a new paradigm on account of the fact that the electronic spins can be polarized optically independent of temperature and even at zero magnetic field. A hint of the possible field dependence (neglecting nuclear relaxation) is elucidated in the simulations of Fig. 3(e). We plot here the integrated transition intensity of the electron spectra as a function of magnetic field, $\mathcal{T}(B_{\rm pol}) = \int_0^{\pi/2} P(\vartheta, B_{\rm pol})$. This suggests that the available NV density of states for hyperpolarization reduces with the increasing field.

In this paper, we furnish an experimental study, reporting in Fig. 4 the measured field dependence of the obtained DNP enhancements under optimal conditions. We use a combination of Helmholtz coil fields and background fringe fields over a wide range (1–70 mT) to systematically map the field dependence under sweeps of the $m_s = +1$ [Fig. 4(a)] and $m_s = -1$ manifolds [Fig. 4(b)], respectively. In actuality, due to amplifier constraints, the data in Fig. 4(a) are obtained in two separate datasets [(1–40 mT) and (30–70 mT)] and pieced together by normalizing overlapping points. We estimate from this an ≈ 11% error through this [marked in the last point of Fig. 4(a)]. We see a sharp field dependence, becoming optimal around $B_{\rm pol} = 38 \pm 4$ mT and falling on either side of this value.

While a quantitative model is still beyond the scope of this paper, we ascribe this behavior to be arising from a competition between two factors with increasing $B_{\rm pol}$: (i) a dominant rise in ^{13}C nuclear T_1 lifetimes and (ii) a fall in the NV center polarization[35] and integrated electron transition probability $\mathcal{T}(B_{\rm pol})$ in the randomly oriented diamond powder. The nuclear T_1 is set for the most part (see Fig. 5) by interactions with the spin bath of paramagnetic electron defects (primarily P1 centers) in the diamond lattice, which present to the ^{13}C nuclei a spin-flipping noise spectral density centered at zero frequency and width given by approximately the inter-electron dipolar coupling. Increasing the field allows the ^{13}C nuclei to sample less of this noise, leading to an increase in T_1 and the ability to buildup polarization for longer times before saturation. This is demonstrated in Fig. 4(c) (*inset*) where we report DNP buildup curves at 15 mT and 20 mT and where the polarization curves saturate at longer times in the latter case. Simultaneously, however, there is a reduced overall NV transition probability $\mathcal{T}(B_{\rm pol})$ at higher fields [Fig. 3(e)] and also [ignored by Fig. 3(e)] a reduction in the number of ^{13}C nuclei directly participating in the DNP process (satisfying the hierarchy $\omega_L \lesssim A$). Due to these factors, we expect a decrease in DNP efficiency at high fields.

Due to these competing factors, we expect that the optimal field value is sample dependent. Overall, however, the low polarizing fields $B_{\rm pol} \approx 40$ mT, and the relatively benign range around this field $\Delta B_{\rm pol} \approx 10$ mT, mean that they are simple to generate

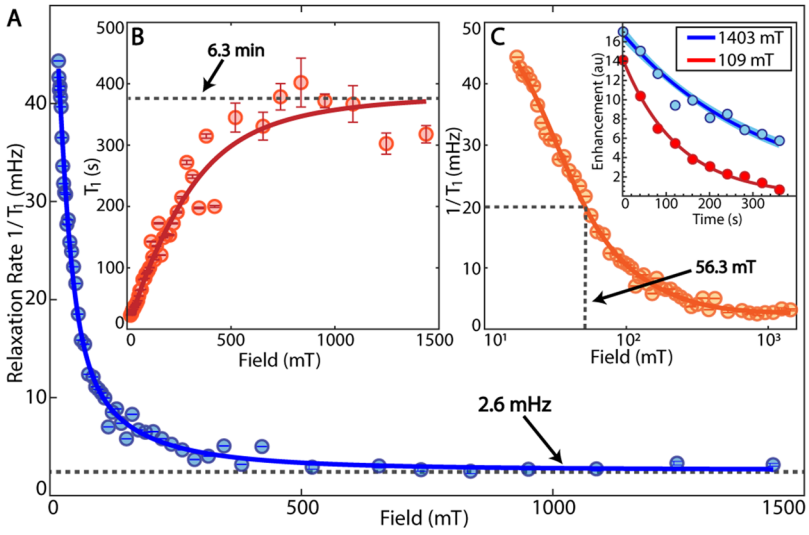

FIG. 5. Lifetimes of hyperpolarized ^{13}C nuclei. (a) *Field dependence* of nuclear relaxation rate $R_1 = 1/T_1$ for hyperpolarized 200 μm particles in Fig. 1(c). There is a steep rise in the relaxation rate at low-fields below $\lesssim$100 mT mediated by interactions with paramagnetic impurities in the lattice. At higher fields, the rate is approximately constant ≈2.6 mHz, allowing efficient retention of hyperpolarization for minute-long periods. The solid line is a Lorentzian fit. Error bars are estimated from monoexponential fits (see the Appendix). (b) Measured T_1 values showing lifetimes >6 min at modest fields. (c) *Knee field* at which the rapid increase in nuclear lifetimes occurs can be quantified as the width in a logarithmic scale, here ≈57 mT. *Inset:* Signal decays at exemplary low and high fields. Shaded are 95% confidence intervals.

through permanent magnets or coils. This feature is key to miniaturization of the hyperpolarizer. Moreover, the MW bandwidth in the optimal $m_s = +1$ manifold to sweep over is relatively narrow $\mathcal{B} \approx 0.35$ GHz around 3.81 GHz. We note that, in contrast, at high fields $B_{pol} \gg 100$ mT, where the mechanism transitions to the standard ISE, one has to contend with a far reduced electron density of states and the $2\Delta \sim 5.9$ GHz wide electron spectral width, which is technologically challenging to sweep over.

VI. LONG TIME HYPERPOLARIZATION RETENTION

While the DNP mechanism is optimum at low fields, we also find that modestly low fields are sufficient to retain this polarization for long periods, with typical cases approaching tens of minutes. We demonstrate this in Fig. 5 by performing a full wide range (B_{relax} = 10 mT–7 T) field dependent mapping of the T_1 relaxation of ^{13}C nuclei in typical diamond microparticles [Fig. 1(c)]. This is achieved by retrofitting a field cycling instrument constructed over a 7 T magnet[36] with our optical hyperpolarizer device. One would naively expect an increase in relaxation rate that falls down as $R_1 \propto 1/B_{relax}$ due to a suppression in electron–nuclear overlaps due to the widening energy gap between the two reservoirs. We find, however, a step-like dependence on the field [see Fig. 5(a)]. There is a strong increase in T_1 beyond a particular knee field ≈57 mT where lifetimes approach 6.3 min and a steep fall below this field [see also Fig. 5(b)]. Knee fields can be most easily quantified in a logarithmic field plot of the relaxation plots [Fig. 5(c)]. We have observed that the dependence in Fig. 5 is typical of diamond particle samples employed for hyperpolarization. In recent companion work to this paper,[37] we have studied the origins of this relaxation behavior by studying various samples under field cycling and with ESR studies to map the electronic concentration. The data are borne out by a model that involves the interaction of the ^{13}C nuclei with paramagnetic defects in the lattice, the knee field value being predominantly set by the dipolar electronic linewidth.[37]

However, the step-like dependence in Fig. 5(a) immediately opens the door to simplification of hyperpolarizer operation and deployment: by rapidly switching the field to $\gtrsim$100 mT after optical pumping by means of an electromagnet, one could retain the polarization for minute-long periods. The behavior in Fig. 5(a) also ensures that the hyperpolarization loss during sample shuttling can be exceedingly small (<1% in our experiments), since it is only the traversal time through ultra-low field regions that predominantly contribute to deleterious loss.

VII. FACTORS SIMPLIFYING MW SWEEPS

We now focus our attention on the factors affecting MW sweeps through the optimal electron bandwidths. For simplicity [see Fig. 6(a)], we distinguish between MW *sweep rates* $\dot{\omega}_r = \mathcal{B}/t_r$, where t_r is the time per sweep, and *repetition rates* $\omega_r = 1/t_r$, which are instead the rate of frequency chirps through the sweep band $\mathcal{B}$. Figure 6(b) shows a typical dependence on the repetition rate, demonstrating a loss of polarization efficiency at slow and fast rates.

Microscopic predictions of the optimal MW sweep rates, and their dependence on the polarizing magnetic field B_{pol}, are once again rather challenging. The Landau–Zener energy gaps and consequently the conditions for adiabatic travel of the level anti-crossings are functions of the applied Rabi frequency Ω_e, NV center orientation, and importantly the hyperfine couplings;[20] given the continuum of couplings and orientations in our sample, the optimal value is analytically difficult to compute. However, as Fig. 6(b) demonstrates, knowledge of this optimal rate is critical to obtaining optimized hyperpolarization enhancements.

In this paper, we experimentally address this question by determining dependence on MW sweep rates for various polarizing fields. Figure 6(c) shows these results, concentrating first on the $m_s = +1$ manifold and employing a frequency comb constructed out of three cascaded MW sweepers. For each polarizing field, we sweep over the full NV ESR band $\mathcal{B}$ given by Fig. 3(c). We find that the MW repetition rates $\omega_r^{(+1)}$ are (to a good approximation) independent of the

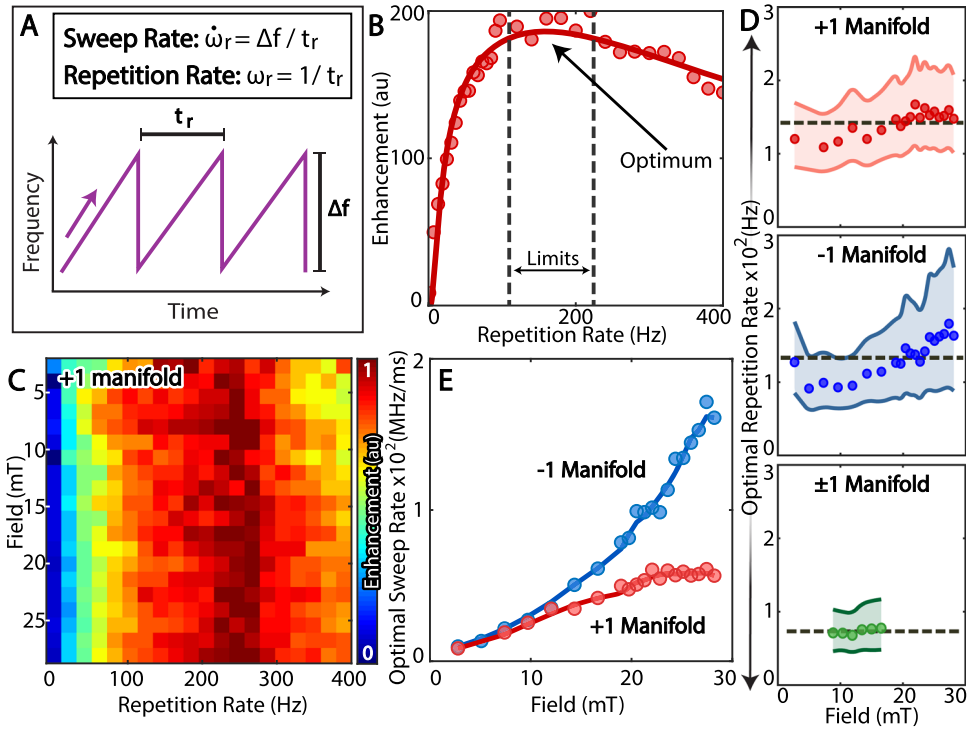

FIG. 6. MW sweep rate dependence of hyperpolarization enhancements. (a) *Definitions.* We distinguish between MW repetition rates ω_r and sweep rates $\dot{\omega}_r$. (b) Exemplary variation with the MW repetition rate at 28.8 mT employing three cascaded MW sources sweeping a bandwidth $\mathcal{B}$ = 384 MHz. The solid line denotes a fit to the microscopic model[20] that qualitatively captures the observed behavior, with dashed lines denoting 5% confidence interval. (c) *Full dataset* as function of field for MW sweeps over the m_s = +1 manifold. Color reflects obtained 7 T DNP enhancements. (d) *Optimal MW repetition rates* ω_r measured for sweeps over the m_s = ± 1 manifolds separately or together. The optimal value is obtained from fits. Data reveal relative field independence of the observed optimal rates, with $\omega_r^{(+1)}$ ≈147 Hz, $\omega_r^{(-1)}$ ≈133 Hz, and $\omega_r^{(\pm 1)}$ ≈73 Hz (dashed lines). The shaded area represents 5% confidence interval around the optimal rates. Data suggest that optimal repetition rates are dominated by the need to sweep each NV once during every optical repolarization cycle. (e) *Optimal sweep rate* $\dot{\omega}_r$ field dependence plotted for sweeps over the m_s = ±1 manifolds individually. Data follow the spread of the underlying electronic spectra in both manifolds [see Fig. 3(d)].

magnetic field. To demonstrate this more clearly, in Fig. 6(d), we extract the optimal repetition rates for fields B_{pol} = 1–30 mT, considering sweeps over the m_s = +1 and −1 manifolds separately, as well as over both manifolds together. These optimal values are obtained from fits of the observed dependence [e.g., solid line in Fig. 6(b)] to the expected behavior from microscopics of the Landau–Zener process,[31] $\varepsilon = A\exp(-\Lambda^2/\omega_r)(1-\exp(-\Omega^2/\omega_r))$. The lines in Fig. 6(d) indicate 95% confidence intervals, showing additionally that the repetition rates exhibit a relatively benign dependence, with width $\Delta\omega_r$ ~50 Hz. In contrast, by plotting the MW sweep rates $\dot{\omega}_r$ in Fig. 6(e), we find that they increase with field and closely follow the underlying spread in the electronic density of states [see Fig. 3(d)].

It is somewhat confounding that the system microscopics conspire to produce relative field independence. Strong hints to the origin of this behavior is provided by the results in Fig. 6(d), where we observe that the optimum repetition rates for sweeps over both m_s = ±1 manifolds simultaneously, $\omega_r^{(\pm 1)}$≈73 Hz ± 29 Hz, are approximately *half* those of sweeps over the individual manifolds, for instance, $\omega_r^{(+1)}$≈147 Hz ± 53 Hz. Indeed, several factors contribute to determining optimal MW rates. There is the need to maximize (i) the polarization transfer efficiency *per* sweep, (ii) the *total* number of sweeps in a period bounded by nuclear T_1, and (iii) the NV electron polarization at the start of every sweep event. Experiments in Fig. 6(b) suggest that the last factor is the most critical, pointing out to relative field independence. Indeed, at the laser powers, we employ the NV repolarization rate $t_{\text{repol}} \sim T_{1e} \approx 1$ ms,[38] and sweeping MWs at a rate $\omega_r \approx 1/(NT_{1e})$ (N = 3 being the number of sweepers) ensures that the largest NV polarization is available to transfer to the ^{13}C nuclei per sweep. This observation once again simplifies hyperpolarizer miniaturization. Sweep times (5–10 ms) are relatively slow and can easily be generated by using microcontrollers to provide voltage ramps that when interfaced with the chip-scale VCOs provide the frequency chirped MWs (see the supplementary material for a miniaturized custom-built frequency-chirp circuit used in our hyperpolarizer).

Indeed, miniaturization is the key behind the ability to cascade multiple frequency sources in a frequency comb in order to provide multiplicative enhancement gains.[31] This works on the principle that while employing a single MW sweeper, the sweep rate also directly sets the total number of sweeps events that can be

applied to the sample. However, the use of multiple sweepers allows one to decouple these two factors: it allows the maintenance of a fixed sweep rate per NV center spin "packet" and hence adiabaticity constraints but increases effectively the number of total number sweeps applied on the spins. Since the total polarization time is bounded by the nuclear T_1, this can lead to a linear increase in the polarization levels by the use of multiple sweepers.[31] However, this increase is operational only in the regime where NV spins are predominantly inhomogeneously broadened and when the sweepers are separated by more than the inhomogeneous electronic linewidth. Indeed, when the number of sweepers is increased further, their spacing in frequency space approaches the homogeneous NV linewidth, and there are no gains in hyperpolarization enhancements to be gained further. We found a saturation in hyperpolarization gains upon using ≈3 sweepers for a ~300 MHz sweep bandwidth.[31]

VIII. BACKGROUND SUPPRESSION VIA SIGN-REVERSALS

The DNP mechanism allows additional SNR gains in the detection of hyperpolarized signals, especially in the presence of large background signals. We refer to "*background*" as those signals that are not arising directly or indirectly from the optically hyperpolarized diamonds. We exploit the observation that the sign of the ^{13}C polarization depends only upon the direction of the MW sweep.[20] Polarization is aligned (anti-aligned) to $\mathbf{B}_{pol}$ for low-to-high (high-to-low) frequency sweeps over the NV ESR spectrum [Fig. 7(a)]. In this paper, we quantify the *inversion fidelity* $\mathcal{F}$ of the sign reversals. We find that when all NV orientations are swept over, the sign reversal is extremely robust, and the amplitude of the ^{13}C polarization inverts to within $(1 - \mathcal{F}) = 2\%$ of its original value [see Fig. 7(b)]. In reality, this is an underestimate of the inversion

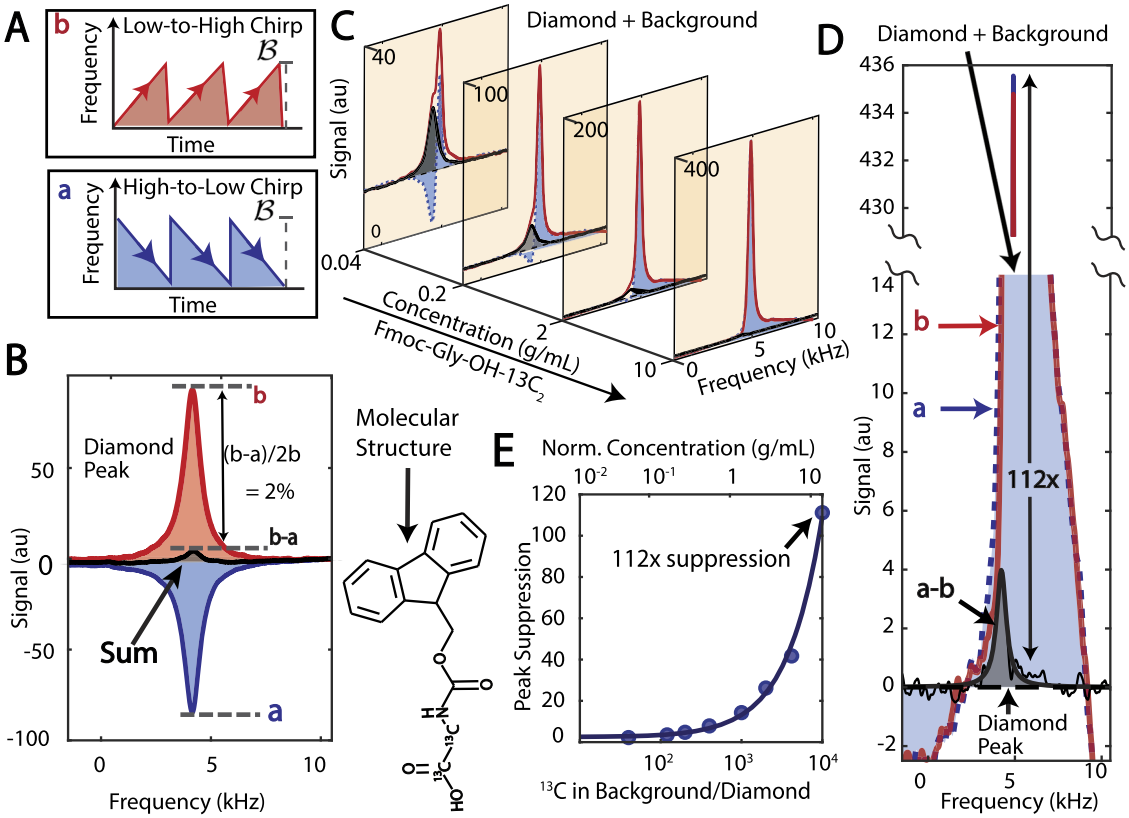

FIG. 7. "Background suppressed" ^{13}C hyperpolarization employing polarization sign reversals. (a) *Schematic of polarization sign control.* Sign of ^{13}C hyperpolarization, aligned or anti-aligned to B_{pol}, depends only on the direction of the MW sweep. (b) *Sign reversal fidelity* $\mathcal{F}$ is evaluated by MW sweeps at B_{pol} = 22 mT. Results demonstrate that the hyperpolarization sign can be reversed on-demand to better than $(1\text{-}\mathcal{F}) = 2\%$. (B) *Background suppression* by exploiting successive sign-reversals of ^{13}C hyperpolarization. Diamond particles in Fig. 1(c) are immersed in increasing concentration (*panels*) of Fmoc-Gly–OH–$^{13}C_2$ ("background") that overlaps the diamond spectrum. Red (blue shaded) line is the obtained spectrum under low-to-high (high-to-low) MW sweeps, each averaged 20 times. Subtracting the results allows one to extract the diamond spectrum (black shaded) although initially indiscernible. Concentrations of the background compound are displayed normalized to 50 diamond particles (see the Appendix). (d) *Zoomed* signal when employing the highest relative concentration [final panel in (c)]. The diamond signal (black) is recovered with high fidelity although initially enveloped by a 112 times stronger background signal, which is now completely suppressed. (e) *Scaling of background suppression* with compound concentration (upper axis). In the final panel of (c), suppression exceeds two orders of magnitude, corresponding to the detection of diamond ^{13}C nuclei immersed in ~10^4 more ^{13}C nuclei in the background (lower axis).

fidelity since it also includes (weak) repolarization during sample shuttling.

This ability to invert hyperpolarization signals on-demand and at high fidelity, with no change of hardware infrastructure, opens the door to background suppression of the DNP signals. Performing successive experiments with alternate MW sweep direction and subtracting the result, one can suppress the background and exclusively recover the DNP signal although it may be initially impossible to discern. Applications for this idea are more powerful in case the polarization from the ^{13}C spins in the diamond powder can be transferred to external liquids, for example, ^{1}H spins in water, through cross polarization[13] or the Overhauser effect.[39] Such hyperpolarized water, with a polarization that is sign invertible at will, could then be used as a bright-field MRI contrast agent in imaging applications, suppressing ^{1}H signals from thermally polarized water in the body and significantly boosting image contrast-to-noise.

In this paper, we demonstrate a restricted proof-of-concept experiment along these lines. We perform DNP on diamond microparticles embedded in a large volume of ^{13}C labeled Fmoc-Gly–OH–$^{13}C_2$, a compound[40] with a chemical shift that completely overlaps with the diamond signal at 7 T. In Fig. 7(c), we increase the concentration of this "background" signal so that the hyperpolarized diamond signal is completely enveloped by it and typically impossible to discern. In fact, in the final panel of Fig. 7(c), the background signal is over 100 times larger than the diamond peak. However, background suppression using polarization sign inversions performs well [see Fig. 7(c)], and we can extract the diamond peak from the 112 times larger background [zoomed-in Fig. 7(d)] with high fidelity.

An instructive representation of SNR gains through a *combination* of hyperpolarization and background suppression is in the lower axis of Fig. 7(e). We are able to discern the diamond peak with high SNR, although every ^{13}C nucleus in diamond is immersed in a background of more than 10^4 more ^{13}C nuclei. This large factor is a multiplicative effect of DNP that renders every ^{13}C in the diamond roughly 100 times "brighter" than 7 T thermally polarized nuclei and polarization sign-reversals that suppress the ^{13}C signatures in the background by over 100 times. The high fidelity recovery of the hyperpolarized signal in Fig. 7(d) indicates that the trend in Fig. 7(e) can be continued further; we expect that one could suppress background signals over 1–2 more orders of magnitude.

IX. CONCLUSIONS

In conclusion, by uncovering new physics underlying the DNP mechanism first introduced in Ref. 20, we have constructed a compact solid-state room-temperature "*optical nanodiamond hyperpolarizer*." The ability to construct such a device rests on a unique confluence of factors underlying the DNP mechanism requiring low fields, low laser, and MW powers, and being robust to field inhomogeneity, optical excitation modes, and MW inhomogeneity. Hyperpolarization is on-demand sign invertible with high-fidelity, can be excited with very modest resources, and retained for long periods approaching tens of minutes. We employed the device to obtain the best reported values of ^{13}C hyperpolarization in diamond micro- and nanoparticles through optical means. We have also highlighted engineering aspects that, leveraging the physics, make our nanodiamond hyperpolarizer device easy to build and operate, and with a small footprint that can retrofit any existing magnet system.

Our work opens the door to many intriguing new future directions. *First*, variants of the hyperpolarizer device could enable efficient polarization transfer relayed from the long-lived surface ^{13}C nuclei to external liquids. While challenges remain requiring paramagnetic defect free surfaces and long relaxation time of surface ^{13}C nuclei of the nanodiamonds, recent materials' advances provide optimism on prospects for external polarization transfer.[41] Importantly, the hyperpolarization so generated optically is replenishable and could also be employed with NV sensors for the optical detection of magnetic resonance.[42,43] This may open new possibilities for miniaturized NMR spectrometers for chemical analysis. *Second*, from a technological standpoint, the device can be easily miniaturized further. A more efficient MW delivery scheme will allow the use of a lower power amplifier that currently occupies the largest footprint. All other MW components can be replaced by chip-scale ones, and a palm-top sized hyperpolarizer can easily be envisioned. Integrating low-field inductive NMR readout[44] into the device will enable an *in situ* measurement of the ^{13}C hyperpolarized signals without the need for sample shuttling. *Finally*, it should be possible to produce similar low field hyperpolarization in other wide bandgap semiconductor materials. Pioneering recent work[45,46] has demonstrated that the V1 defect center in silicon carbide can be hyperpolarized through infrared light. Employing these spins for DNP will allow *in vivo hyperpolarization* of ^{29}Si nuclei and background-free imaging of nanoparticles targeting disease locations.

SUPPLEMENTARY MATERIAL

See the supplementary material for more details about the construction of the miniature hyperpolarizer device, including the electronics for frequency sweep generation required to excite dynamic nuclear polarization (DNP). We also characterize the performance of the device under field and MW inhomogeneity and provide the details of an integrated Hall probe system to measure the magnetic field at the site of the polarizer device. This aids in its use as a retrofit for the existing NMR and MRI systems. We characterize enhancement levels when the diamond particles are hyperpolarized while being immersed in different solutions, including solvents, and biological liquids such as blood and saline. Finally, we detail measurements of the ^{13}C lifetimes in diamond as a function of magnetic field, and for completeness, we include an overview of the DNP mechanism operational in our device.

ACKNOWLEDGMENTS

We are thankful to D. Budker, B. Blümich, S. Conolly, A. Gali, F. Jelezko, M. Lustig, C. Ramanathan, D. Sakellariou, O. Shenderova, and J. Wratchrup for insightful conversations. We acknowledge technical contributions from X. Cai, S. Le, G. Li, A. Lin, X. Lv, T. McNelley, P. Raghavan, I. Yu, and R. Zhao. C.A.M. acknowledges support from the National Science Foundation through Grant Nos. NSF-1547830 and NSF-1903839 and from Research Corporation for Science Advancement through a FRED Award.

APPENDIX: MATERIALS AND METHODS

1. Hyperpolarizer construction

The hyperpolarizer [Figs. 1(a) and 2] is a stand-alone device fully operational at room-temperature, composed of nonmagnetic solid-state components and requiring almost zero user maintenance. We choose a modular design that allows a compact and rapid assembly of the various components (see Fig. 8). The device has a small footprint (12 in. × 10 in. × 10 in.) and is light weight (<10 lb), making it ultraportable and compatible with any NMR spectrometer. This small hyperpolarizer is testament to the technological ease of optical DNP at low fields.

The aluminum chassis supports three distinct modular blocks (see Fig. 2): optics, MW sweep generation, and a sample holder that contains the diamond particles to be hyperpolarized (Fig. 8). The densely packed and double-sided design supports easily customizable modalities for sample placement and removal. For instance, the device can contain a hollow bore to allow shuttling of the sample into a high field NMR magnet. For more experiments, we employ a miniature 1 W 520 nm diode laser (Lasertack PD-01289) in a feedback loop with an integrated thermoelectric cooler for adequate thermal control (TE Inc. TE-63-1.0-1.3). Very few optical components are required [see Fig. 8(b)]: an aspheric lens and a set of anamorphic prisms collimate the beam to a circular 4 mm diameter. Two mirrors redirect the beam toward the sample, typically irradiating it from below. We note, however, that the modular design of the device engenders the use of multiple laser sources (fiber coupled with Thorlabs M35L01) to illuminate large masses of the sample or to ensure better illumination coverage on the densely packed diamond powder. We have employed up to nine sources simultaneously on the sample at a total power of ~400 mW/mm^3 without significant sample heating.

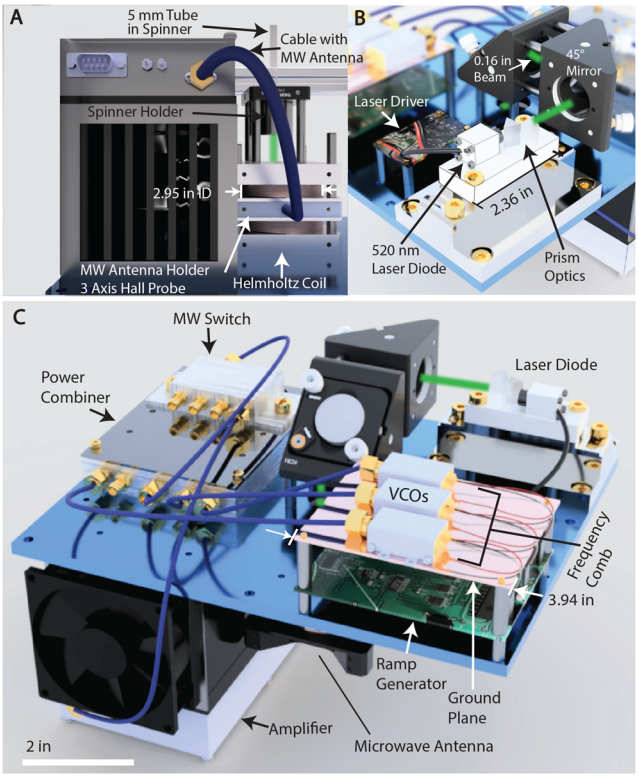

FIG. 8. Nanodiamond hyperpolarizer schematic (to scale) showing component parts assembled on a single 10 in. × 10 in. aluminum plate (blue). (a) *Sample attachment*. Diamond particles to be hyperpolarized are placed at the confluence of the laser and MW excitation in a weak polarizing field generated by the Helmholtz coil pair. Amplified MWs are delivered by means of a stubbed loop antenna [see Fig. 4(d)]. (b) *Optical excitation* is provided by a small (2.36 in.) 520 nm 1 W laser diode placed on the plate underside. Minimal optics direct the beam to the sample. Alternatively, multi-mode optical fibers can deliver the light from one or more laser diodes mounted in the device. (c) *MW generation and excitation* circuitry (also on the plate underside) involves miniature VCO sources interfaced with a custom-built voltage ramp generator to produce the MW frequency sweeps. Chirped MWs are subsequently power combined, amplified, and finally delivered to the MW antenna. The ultracompact, modular, design allows easy customization and enhances device portability.

Microwaves are generated by miniature voltage controlled oscillator (VCO) sources (Minicircuits ZX95-3800A+, 1.9–3.7 GHz, output power $p = 3.1$ dBm). Frequency sweeps are produced by controlling the VCO frequency by a homebuilt quad-channel voltage ramp generator controlled by a PIC microprocessor (PIC30F2020). Figure 8(c) shows the connected VCOs mounted on a copper sheet that serves as a good ground plane. Given the relatively slow MW sweeps required, $\omega_r \approx 164$ Hz, and translating to sweep times of 6 ms for the typical sweep bandwidths, $\mathcal{B} = 100$ MHz–1 GHz, the 50 kHz clock speeds of the microprocessor provide sufficiently fast control for the sweep circuitry. The sweep generator employs dual multiplying digital-to-analog convertors (MDACs, Linear Technology LTC1590) to generate the sawtooth voltage ramps. The sweeps from the individual sources are time-cascaded, generating a MW frequency comb that sweeps different parts of the NV ESR spectrum at once. This allows multiplicative gains in the obtained DNP enhancements. The VCO outputs are power-combined (Minicircuits ZN4PD1-63HP-S+, $p = 2.2$ dBm), passed through a high-isolation switch (Minicircuits ZASWA- 2-50DR+, $p = -0.46$ dBm), and delivered to a low-cost amplifier (Minicircuits ZHL16W–43S+, $p = 37.9$ dBm) that transmits the microwave irradiation to the sample via a stubbed loop antenna (4 mm diameter, reflected power $p = 36.3$ dBm, and radiation efficiency = 24%). The radiated MW powers required are extremely low, estimated to be below 1.5 W. To estimate the Rabi frequency, we assume an upper limit of microwave output power $P \approx 1.5$ W at a frequency $\nu = 3$ GHz. Since the circuit is broadband, the magnetic energy is at most $W_B = P/\nu$ and equal to $w_B V = \frac{B^2}{2\mu_0}\frac{4\pi}{3}R^3$, where w_B is energy density of the magnetic field and we approximate the volume by a sphere with radius $R = 2$ mm. To generate the weak field B_{pol} used for hyperpolarization, as described in Fig. 4(a), we employ a single axis Helmholtz coil (25 turns, ten layers, 0.8 mm diameter) mounted around the sample, generating 14 mT fields with ≈2 A of current and with minimal heating. The coil also helps in the hybrid scenario supplementing detection magnet fringe fields. A set of three small Hall sensors (AsahiKASEI EQ-731L, magnetic sensitivity 65 mV/mT) are placed in the polarizing window near the sample, which provides an *in situ* measurement of the field. A simple feedback loop can match the field with any desired value.

2. Materials

While we have focused entirely on the physics of the hyperpolarization mechanism and the construction of the hyperpolarizer device, the material properties of the diamond particles employed can themselves play a critical role in setting the ultimate hyperpolarization levels. The particles employed for hyperpolarization can be high-pressure high temperature (HPHT) and chemical vapor deposition (CVD) grown and generally have a high density (~1–10 ppm) of NV centers.[47] In Ref. 30, we studied these material factors in detail across different dimensions including electron irradiation doses, sample annealing conditions, and particle size. We observed that the quality of the lattice plays a critical role and sets directly both the NV centers T_1 and T_2 coherence time, but also the ^{13}C T_1 lifetimes. In general, a more pristine lattice free from paramagnetic defects can lead to higher hyperpolarization enhancement levels. Through combined ESR and NMR studies, we demonstrated that rapid annealing of the diamond particle sample at a high temperature (1700–1800 °C for 15 min) can substantially relieve lattice damage stemming from electron irradiation and improve the hyperpolarization levels by an order of magnitude when compared to standard annealing conditions (850 °C for 2 h). We refer the reader to Ref. 30 for a more detailed exposition on these aspects.

3. Experimental methods

In the experiments of Figs. 1(b)–1(e), we employed, in the hyperpolarizer device, a fiber coupled excitation involving an octagonal arrangement of eight 800 mW diode lasers to ensure that all particle surfaces were maximally exposed to illumination. The field dependence experiments in Fig. 4(a) over the wide field range were obtained as a combination of two datasets accessing (1–40 mT) and (30–70 mT) ranges and normalizing points in the overlapping regime. From this, we obtain the error bar of 11% indicated in Fig. 4(a). For the latter range, we employed the Synergy DCRO330500 VCOs and AR50S1G6 amplifier combination. For background suppression experiments in Fig. 7, Fmoc-Gly–OH–$^{13}C_2$ was successively added in a NMR tube containing 0.5 ml DMSO (Fisher Scientific) and 50 particles of 200 μm diamonds at the beginning. After reaching saturation at 1 g/ml, the amount of diamonds was halved from step to step. The concentrations in Fig. 7(c) are displayed normalized to 50 particles. The calculated ratio between the number of ^{13}C atoms in Fmoc-Gly–OH–$^{13}C_2$ and diamond was based on mass considerations. Considering that the Fmoc-Gly–OH–$^{13}C_2$ mass m_F (g), and having molar mass M_F = 299.29 g/mol, the molar mass of diamond M_D = 12.01 g/mol, the density of diamond ρ = 3.52 g/cm^3, the edge length of the truncated octahedral crystallites a = 87 ± 3 μm, and the number of diamonds n, the ratio of ^{13}C nuclei outside the diamond to within it can be calculated as $\frac{m_F M_D}{8\sqrt{2}a^3\rho n M_F}\frac{100}{1.1}$ [upper axis in Fig. 7(e)].

Experiments in Fig. 5 are carried out by interfacing the hyperpolarizer with a mechanical field cycling instrument constructed over a 7 T detection magnet and consisting of a sensitive conveyor belt actuator stage (Parker HMRB08) with 50 μm precision and 1.5 m travel range in the fringe field of the magnet, allowing a rapid (~700 ms) and wide field sweep range from 10 mT to 7 T.[36]

REFERENCES

[1] T. R. Carver and C. P. Slichter, Phys. Rev. **92**, 212 (1953).
[2] A. Abragam and M. Goldman, Rep. Prog. Phys. **41**, 395 (1978).
[3] R. Ernst, G. Bodenhausen, and A. Wokaun, *Principles of Nuclear Magnetic Resonance in One and Two Dimensions* (Clarendon Press Oxford, 1987).
[4] J.-H. Ardenkjaer-Larsen, G. S. Boebinger, A. Comment, S. Duckett, A. S. Edison, F. Engelke, C. Griesinger, R. G. Griffin, C. Hilty, H. Maeda *et al.*, Angew. Chem., Int. Ed. **54**, 9162 (2015).
[5] T. W. Kornack, R. K. Ghosh, and M. V. Romalis, Phys. Rev. Lett. **95**, 230801 (2005).
[6] E. A. Donley, in *2010 IEEE Sensors* (IEEE, 2010), pp. 17–22.
[7] A. Ajoy and P. Cappellaro, Phys. Rev. A **86**, 062104 (2012).
[8] M. Goldman, *Spin Temperature and NMR in Solids* (Clarendon Press, Oxford, 1970).
[9] A. De Luca and A. Rosso, Phys. Rev. Lett. **115**, 080401 (2015).
[10] J. H. Ardenkjaer-Larsen, B. Fridlund, A. Gram, G. Hansson, L. Hansson, M. H. Lerche, R. Servin, M. Thaning, and K. Golman, Proc. Natl. Acad. Sci. U. S. A. **100**, 10158 (2003).
[11] T. Maly, G. T. Debelouchina, V. S. Bajaj, K.-N. Hu, C.-G. Joo, M. L. MakJurkauskas, J. R. Sirigiri, P. C. A. van der Wel, J. Herzfeld, R. J. Temkin, and R. G. Griffin, J. Chem. Phys. **128**, 052211 (2008).
[12] M. Rosay, L. Tometich, S. Pawsey, R. Bader, R. Schauwecker, M. Blank, P. M. Borchard, S. R. Cauffman, K. L. Felch, R. T. Weber *et al.*, Phys. Chem. Chem. Phys. **12**, 5850 (2010).
[13] X. Ji, A. Bornet, B. Vuichoud, J. Milani, D. Gajan, A. J. Rossini, L. Emsley, G. Bodenhausen, and S. Jannin, Nat. Commun. **8**, 13975 (2017).
[14] F. Jelezko and J. Wrachtrup, Phys. Status Solidi A **203**, 3207 (2006).
[15] R. Fischer, C. O. Bretschneider, P. London, D. Budker, D. Gershoni, and L. Frydman, Phys. Rev. Lett. **111**, 057601 (2013).
[16] P. London, J. Scheuer, J.-M. Cai, I. Schwarz, A. Retzker, M. Plenio, M. Katagiri, T. Teraji, S. Koizumi, J. Isoya *et al.*, Phys. Rev. Lett. **111**, 067601 (2013).
[17] D. Abrams, M. E. Trusheim, D. R. Englund, M. D. Shattuck, and C. A. Meriles, Nano Lett. **14**, 2471 (2014).
[18] J. Scheuer, I. Schwartz, Q. Chen, D. Schulze-Sünninghausen, P. Carl, P. Höfer, A. Retzker, H. Sumiya, J. Isoya, B. Luy *et al.*, New J. Phys. **18**, 013040 (2016).
[19] T. Zapata, N. Bennett, V. Struzhkin, Y. Fei, F. Jelezko, J. Biskupek, U. Kaiser, R. Reuter, J. Wrachtrup, F. A. Ghannam *et al.*, arXiv:1702.06854 (2017).
[20] A. Ajoy, K. Liu, R. Nazaryan, X. Lv, P. R. Zangara, B. Safvati, G. Wang, D. Arnold, G. Li, A. Lin *et al.*, Sci. Adv. **4**, eaar5492 (2018).
[21] T. M. Hoang, J. Ahn, J. Bang, and T. Li, Nat. Commun. **7**, 12250 (2016).
[22] A. M. Schrand, H. Huang, C. Carlson, J. J. Schlager, E. Ōsawa, S. M. Hussain, and L. Dai, J. Phys. Chem. B **111**, 2 (2007).
[23] S.-J. Yu, M.-W. Kang, H.-C. Chang, K.-M. Chen, and Y.-C. Yu, J. Am. Chem. Soc. **127**, 17604 (2005).
[24] Y.-R. Chang, H.-Y. Lee, K. Chen, C.-C. Chang, D.-S. Tsai, C.-C. Fu, T.-S. Lim, Y.-K. Tzeng, C.-Y. Fang, C.-C. Han *et al.*, Nat. Nanotechnol. **3**, 284 (2008).
[25] See https://www.youtube.com/watch?v=IjnMh-sROK4 for the video showing ultraportable nanodiamond hyperpolarizer.
[26] E. Rej, T. Gaebel, T. Boele, D. E. Waddington, and D. J. Reilly, Nat. Commun. **6**, 8459 (2015).
[27] C. O. Bretschneider, Ü. Akbey, F. Aussenac, G. L. Olsen, A. Feintuch, H. Oschkinat, and L. Frydman, ChemPhysChem **17**, 2691 (2016).
[28] C. Wan, M. Scala, G. Morley, A. A. Rahman, H. Ulbricht, J. Bateman, P. Barker, S. Bose, and M. Kim, Phys. Rev. Lett. **117**, 143003 (2016).
[29] Y. Ma, T. M. Hoang, M. Gong, T. Li, and Z.-q. Yin, Phys. Rev. A **96**, 023827 (2017).
[30] M. Gierth, V. Krespach, A. Shames, P. Raghavan, E. Druga, N. Nunn, M. Torelli, R. Nirodi, S. Le, R. Zhao *et al.*, arXiv:1911.03322 (2019).
[31] A. Ajoy, R. Nazaryan, K. Liu, X. Lv, B. Safvati, G. Wang, E. Druga, J. Reimer, D. Suter, C. Ramanathan *et al.*, Proc. Natl. Acad. Sci. U. S. A. **115**, 10576 (2018).
[32] P. R. Zangara, S. Dhomkar, A. Ajoy, K. Liu, R. Nazaryan, D. Pagliero, D. Suter, J. A. Reimer, A. Pines, and C. A. Meriles, Proc. Natl. Acad. Sci. U. S. A. **116**, 2512 (2019).

[33]Q. Chen, I. Schwarz, F. Jelezko, A. Retzker, and M. Plenio, Phys. Rev. B **92**, 184420 (2015).
[34]A. Henstra and W. T. Wenckebach, Mol. Phys. **112**, 1761 (2014).
[35]M. L. Goldman, A. Sipahigil, M. Doherty, N. Y. Yao, S. Bennett, M. Markham, D. Twitchen, N. Manson, A. Kubanek, and M. D. Lukin, Phys. Rev. Lett. **114**, 145502 (2015).
[36]A. Ajoy, X. Lv, E. Druga, K. Liu, B. Safvati, A. Morabe, M. Fenton, R. Nazaryan, S. Patel, T. F. Sjolander, J. A. Reimer, D. Sakellariou, C. A. Meriles, and A. Pines, Rev. Sci. Instrum. **90**, 013112 (2019).
[37]A. Ajoy, B. Safvati, R. Nazaryan, J. Oon, B. Han, P. Raghavan, R. Nirodi, A. Aguilar, K. Liu, X. Cai *et al.*, Nat. Commun. **10**, 5160 (2019).
[38]A. Jarmola, V. Acosta, K. Jensen, S. Chemerisov, and D. Budker, Phys. Rev. Lett. **108**, 197601 (2012).
[39]G. Navon, Y.-Q. Song, T. Room, S. Appelt, R. Taylor, and A. Pines, Science **271**, 1848 (1996).
[40]J. L. Harris, B. J. Backes, F. Leonetti, S. Mahrus, J. A. Ellman, and C. S. Craik, Proc. Natl. Acad. Sci. U. S. A. **97**, 7754 (2000).
[41]P. Fernandez-Acebal, O. Rosolio, J. Scheuer, C. Muller, S. Muller, S. Schmitt, L. P. McGuinness, I. Schwarz, Q. Chen, A. Retzker *et al.*, Nano Lett. **18**, 1882 (2018).
[42]N. Aslam, M. Pfender, P. Neumann, R. Reuter, A. Zappe, F. F. de Oliveira, A. Denisenko, H. Sumiya, S. Onoda, J. Isoya, *et al.*, Science **357**, 67 (2017).
[43]D. R. Glenn, D. B. Bucher, J. Lee, M. D. Lukin, H. Park, and R. L. Walsworth, Nature **555**, 351 (2018).
[44]H. Lee, E. Sun, D. Ham, and R. Weissleder, Nat. Med. **14**, 869 (2008).
[45]A. L. Falk, P. V. Klimov, V. Ivády, K. Szász, D. J. Christle, W. F. Koehl, Á. Gali, and D. D. Awschalom, Phys. Rev. Lett. **114**, 247603 (2015).
[46]R. Nagy, M. Widmann, M. Niethammer, D. B. R. Dasari, I. Gerhardt, O. O. Soykal, M. Radulaski, T. Ohshima, J. Vučković, N. T. Son, I. G. Ivanov, S. E. Economou, C. Bonato, S.-Y. Lee, and J. Wrachtrup, Phys. Rev. Appl. **9**, 034022 (2018).
[47]V. N. Mochalin, O. Shenderova, D. Ho, and Y. Gogotsi, Nat. Nanotechnol. **7**, 11 (2012).